

Double-locked nucleation and growth kinetics in Nb-H thin films

Kai Nörthemann and Astrid Pundt*

University of Göttingen, Institut für Materialphysik, Friedrich-Hund-Platz 1, D-37077 Göttingen, Germany

(Received 30 September 2010; published 11 April 2011)

The kinetics of hydride precipitation in epitaxial Nb films are studied by means of scanning tunneling microscopy (STM) using hydrogen gas loading. Due to the clamped state of thin films, hydride formation results in strong unidirectional out-of-plane film expansion that can be easily detected with STM. Hydrides are found to initially form with cylindrical morphology, leading to typical surface topographies. Their localized expansion allows the analysis of the hydride lattice matching, which is coherent (H1) at the initial stages and semicoherent (H2) at later stages. The volume fraction of H1 and H2 precipitates changes with time. At initial stages, the coherent precipitates dominate, while at later stages semicoherent precipitates become the dominant ones. The relative occurrence of H1 and H2 is bimodal. A maximum occurrence of 30–40 nm sized H1 hydrides is found, which is related to coherency stress between the hydride and the Nb matrix hindering a further hydride growth. It is further demonstrated that for Nb-H films adhered to substrates, the system can be locked in the two-phase region of the phase diagram (here at 10^{-4} Pa at about 50% of hydride). This is different from bulk Nb-H, where the complete sample transforms into a hydride when the hydride formation equilibrium pressure is exceeded. Impact parameters on the lateral hydride arrangement are studied. The impact of the Pd-island surface coating and the intrinsic dislocation network on the precipitation density and arrangement appear to be negligible. However, the substrate miscut and, thus, the surface roughness exhibit a strong influence on hydride nucleation. The H1 hydride arrangement along (111) and the directed H2 hydride growth along (111) are governed by the elastically soft matrix lattice orientations.

DOI: [10.1103/PhysRevB.83.155420](https://doi.org/10.1103/PhysRevB.83.155420)

PACS number(s): 68.55.Nq, 81.30.Mh, 68.37.Ef, 47.11.Fg

I. INTRODUCTION

Nucleation and growth kinetics in thin films clamped to substrates are expected to differ from that of bulk systems, mainly because of (i) the limited material supply, which is influenced by the presence of the film surface and the film substrate interface, and (ii) the lateral mechanical stress contributions, which may hinder the phase transformation. Stress contributions can be differentiated into those originating from precipitate volume expansion (elastic stress) and from the lattice matching (coherency stress) compared to the film matrix. Only in the fictitious case of a phase transformation without volume change and zero initial stress can such an effect be neglected. Furthermore, the related microstructure of an individual thin film is also assumed to influence nucleation and growth. All types of defects, namely borders of growth terraces, dislocation cores, or grain boundaries impinging the film surface, might act as heterogeneous nucleation centers.¹

A phenomenological model describing transformation kinetics in materials is that of Johnson, Mehl, Avrami, and Kolmogoroff (JMAK).^{2–5} The kinetic model is based on the assumptions that (i) the phase transformation occurs by nucleation and growth processes, (ii) nucleation sites are randomly distributed throughout the regarded volume, (iii) the nucleus critical size is zero, and (iv) the growth and the nucleation laws are assumed to be given priority.⁶ The description also includes grain boundaries, interfaces, or edges. According to the JMAK model, the describing formula is essentially

$$X(t) = \left\{ 1 - \exp \left[- \left(\frac{t}{\tau} \right)^n \right] \right\}, \quad (1)$$

with the time-dependent volume fraction $X(t)$ of the transformed phase, τ the time of phase appearance, and the Avrami

exponent n . The JMAK equation usually accounts for complete phase transition, resulting in a complete transition of the reaction volume into the final phase. For some cases, the Avrami exponent provides information about the nucleation rate and precipitate shape.² It also allows us to determine the contributions of nucleation and growth, since n can be split into nucleation n_n and growth n_g contributions. Christian published tables of values for n , separated by the type of transformation. While for discontinuous precipitation or interface controlled growth n varies between 1 and 4, for the diffusion controlled growth it ranges between 0.5 and 2.5.² As Johnson mentioned, the tables are not meant to be exhaustive; external surfaces, for example, reduce n by up to 1 for a foil, and by up to 2 for a wire.² A reduction of up to 1 is expected for the thin films regarded in this paper.

The JMAK description has been discussed in the past.^{6–9} It has been criticized due to the fact that already-transformed material is also allowed to transform (“extended volume and phantom nuclei”)—so basically, the short time behavior should be well described and the transformed volume is assumed to be overestimated. However, as Michaelsen *et al.* claimed, Erukhimovitch’s treatment was erroneous and JMAK theory continues to constitute a valid description. Also, Tomellini and Fonzoni support this statement, extending it even to thin-film growth.¹⁰ It is beyond the scope of this paper to discuss the suitability of JMAK kinetics in general. In this study, we will focus on the experimental results obtained on thin films, which will be discussed with respect to JMAK kinetics.

Phase transformations in thin films have been studied intensively, for example on foils of amorphous materials without substrates.^{11,12} But for thin films attached to substrates, detailed experimental results on nucleation and growth kinetics are rare.^{13,14} X-ray diffraction is often applied to monitor

phase transformations, but peak intensities of textured and phase-transformed films are difficult to translate into the contribution of the transformed volume. Furthermore, small nuclei are undetectable by x-ray diffraction due to their lattice coherency.¹⁵ The lack of experimental results might also result from the difficulties in experimental studies on the morphological evolution of precipitates in thin films. Since mechanical stress essentially influences precipitation in thin films, these studies require a remaining substrate to fully describe the thin-film–substrate condition. Thus, *in situ* electron microscopy studies on thin foils do not reflect conventional thin-film conditions because of the missing substrate. Moreover, they are influenced by additional free surfaces needed for transmission electron microscopy (TEM) imaging. Even in cross-section geometry, which conserves the substrate, the total film thickness of several tens of nm affects the nucleation and growth conditions. Then again, conventional *ex situ* experiments on samples frozen in different stages of nucleation and growth require films with exactly the same microstructure and initial mechanical stress conditions. For thin films, this is hard to achieve because of the numerous different defect types occurring, especially when misfitting precipitates are generated. For the sake of clarity, chronological *in situ* studies should be performed on one and the same film.

In this paper, we use hydrogen-metal binary alloys as a model system, which offers various advantages when studying phase-transformation kinetics.¹ Because of the hydrogen absorption on interstitial lattice sites, hydrogen diffusion is relatively fast. Diffusion constants of 10^{-8} cm²/s are measured for H in Nb at room temperature.¹⁶ Thus, alloying can be performed at ambient temperature. The hydrogen content c_H can be increased by simply increasing the hydrogen gas pressure p_H . This allows measuring a complete isothermal cut of the phase diagram using one sample.

For bulk material, the linear dependence of hydrogen concentration and hydrogen gas pressure is given by Sievert's law $c_H = S\sqrt{p_H}$, where S is the hydrogen solubility for the bulk solid solution. For thin films, the hydrogen solubility constant S is changed compared to the bulk system, mainly because of mechanical stress.¹⁷ Furthermore, in bulk materials the lattice expands linearly with the hydrogen concentration. For Nb-H it is $\frac{d}{d_0} = 0.058c_H$.^{18–20} However, for thin films, H concentration and lattice expansion are not so simply related.^{1,21} Only at low concentrations is a linear dependency detected. The lattice expansion is unidirectional and larger in comparison to bulk, due to the film's clamped condition, where in-plane expansion is mostly not possible.

Because of transverse contraction, the out-of-plane expansion of the clamped thin film is much larger than the expansion of one lattice direction in bulk. In the linear elastic regime, an expansion of $\frac{d}{d_0} = 0.13c_H$ is calculated.^{21–24} This strong out-of-plane expansion is confirmed by *in situ* x-ray diffraction by Yang *et al.* on Pd/Nb-H multilayers and by Laudahn *et al.* on Nb-H thin films.^{21,24} Microstructural defects such as grain boundaries, dislocations, and surfaces change the measured hydrogen solubilities and the solubility limits. The increased mechanical stress is released by plastic deformation, which leads to a further change of the lattice expansion depending on the sample morphology and the film-substrate adhesion.^{1,17}

The solubility limit of the bcc α phase in bulk Nb is $c_{\alpha, \text{lim}} = 0.06$ H/Nb at 300 K.²⁵ Above this concentration, a two-phase region consisting of the α phase and a bcc β -hydride phase exists up to 0.7 H/Nb. Above 0.7 H/Nb, the Nb-H film is simply in the β -hydride phase. The related phase-transition hydrogen gas pressure at 293 K is 2×10^{-5} Pa.²⁶ For thin films, phase-boundary concentrations and phase-transition pressures can change, depending on stress contributions and microstructure of the respective film.^{1,17} For epitaxial Nb films on (11 $\bar{2}$ 0) sapphire, Dornheim determined phase boundaries of $c_{\alpha, \text{lim}} = 0.06$ H/Nb and $c_{\beta, \text{lim}} = 0.6–0.7$ H/Nb for 100 nm Nb, or $c_{\alpha, \text{lim}} = 0.26$ H/Nb and $c_{\beta, \text{lim}} = 0.64–0.69$ H/Nb for 35 nm Nb, respectively.²⁷ A phase-transition pressure of 6×10^{-5} Pa was determined for epitaxial Nb films, which was found to be independent of the film thickness.²⁸

To summarize, in thin films both the hydrogen concentration and the lattice expansion increase with increasing hydrogen gas pressure. Thus, *in situ* studies using the same Nb-H sample can be performed by controlling the hydrogen partial pressure.

Scanning tunneling microscopy (STM) is a powerful tool to study the hydride precipitation in thin films via surface topography changes.²⁸ Because of the strong out-of-plane expansion during hydride formation in thin films, hydride precipitation results in local surface topography changes. As was recently shown, the lateral extension of these topographies correlates to the hydride's lateral size.²⁸ Furthermore, the topography's height is generated by the hydride shape and vertical extension.²⁸

This paper focuses on the nucleation and growth of hydrides in epitaxial Nb thin films. By increasing the environmental hydrogen partial pressure, the hydrogen concentration in the films is stepwise increased. Above the solubility limit of the α phase, this leads to the formation of hydrides. Hydride nucleation and growth is expected to be affected by microstructural contributions such as domain boundaries and a misfit dislocations network accounting for the lattice mismatch between the film and the substrate. Because of the absence of grain boundaries in epitaxial films, this contribution to hydride nucleation and growth can be excluded.

The chronological film surface topography development was investigated by performing experimental STM surface measurements on Nb films of different thickness and by finite-element modeling. The combination of the results provides an inside view of the precipitation and growth of hydrides in epitaxial Nb thin films. Experimental findings are discussed with regard to the JMAK kinetics.

II. EXPERIMENTAL DETAILS

Epitaxial Nb films of 20, 40, 70, and 80 nm thickness were deposited onto (11 $\bar{2}$ 0)-oriented sapphire substrates by ion-beam sputtering in an ultrahigh-vacuum (UHV) chamber with a base pressure of 10^{-8} Pa. During deposition, the Ar pressure was kept at 10^{-3} Pa. A substrate temperature of 800 °C was chosen for Nb-film deposition to allow for epitaxial film growth.²⁹ The substrate temperature was reduced to 40 °C before a monolayer of palladium (Pd) was deposited. This low temperature inhibits Pd interdiffusion to the Nb film and vice versa. On the Nb surface, Pd forms tiny islands of 3 nm lateral

diameter and two-layer height, as determined by STM surface topography measurements.

The Pd islands facilitate the hydrogen adsorption and absorption in the Nb film. The hydrogen partial pressure never exceeded 10^{-5} Pa during deposition, avoiding the risk of unregulated hydride formation during film deposition.

Small metal deposition rates of 0.6 nm/min for Nb and 1 nm/min for Pd were chosen. As Wildes *et al.* have proven for similar conditions by the evaporation technique, epitaxial Nb films grow on sapphire substrates with a strong lattice orientation relation ($\{11\bar{2}0\}$ sapphire \parallel $\{110\}$ niobium).²⁹ The remaining lattice misfit to the substrate results in a dislocation network with an average dislocation spacing of 2.5 nm when complete strain relaxation is assumed.³⁰ For evaporated Nb films, this spacing was experimentally confirmed by Grier *et al.* using high-resolution electron microscopy.³⁰ For dc-magnetron sputter-deposited Nb films, Tricker and Stobbs reported a spacing of 8–13 nm, resulting from lattice-mismatch accommodation in $[\bar{1}12]$ directions only.³¹ Texture measurements on the sputter-deposited films confirm the strong orientation relation also for the cathode beam sputter-deposited films. STM topography images of the sputtered Nb films confirm the existence of a dislocation network. Edge components of the dislocation network are visible as glide steps at the film surface. Glide steps are limited by the threading dislocations, which connect the misfit dislocation at the film-substrate interface with the film surface. These components mainly possess screw character. A mean screw dislocation spacing of 38 nm was determined, which is even larger than the spacing reported by Tricker and Stobbs.³¹ A screw dislocation density of $7 \times 10^{10} \text{ cm}^{-2}$ was measured. This relatively low dislocation density indicates an incomplete stress release. Furthermore, it is very likely that just a fraction of the dislocations is visible by traces at the film surface.

Two different sapphire substrates with miscuts (a) better than 0.1° and (b) better than 0.2° were used to study the miscut's influence on hydride precipitation. The larger miscut of substrates results in more surface steps and smaller terrace widths on the as-deposited Nb film. All STM studies were performed after sample preparation without breaking the UHV conditions. After deposition, the background pressure was 10^{-5} Pa in the sputter chamber and better than 10^{-7} Pa in the STM chamber. For measurements in the STM chamber a constant hydrogen gas flow keeps the hydrogen partial pressure automatically at a constant value. All STM images were taken at 300 K. In STM measurements, the scanning direction can also be regarded as a time axis, imaging subsequent states of the film during one scan. Only when precipitation and growth occurs on a much longer time scale than the scan itself can time-independent images be obtained. In the two-phase region of the Nb-H film, a day time scale is needed to reach the two-phase equilibrium, when the loading is done not directly after film preparation. There, STM images usually represent the actual state of nucleation and growth. In the α phase, an equilibrium state is reached within three scans. As shown before, the time scale is driven by the hydrogen supply at the film surface, and changes are mainly due to hydrogen absorption in the film.³² This hydrogen absorption can be directly monitored by substrate bending when the used substrate is thin.³² Because we like to consider only film

expansion (and no substrate bending) in this work, a thick substrate with a thickness of 1 mm was chosen. For this thickness, substrate bending effects can be neglected.

III. FINITE-ELEMENT MODELING

To study the origin of the experimentally obtained surface topographies, finite-element-method calculations were performed. For all calculations, the COMSOL MULTIPHYSICS³³ program package was used.

As a model, three-dimensional Nb-films of different film thicknesses were fixed to a semi-infinite and rigid substrate. Elastic properties of niobium and sapphire were implemented.³³ For simplicity, the films were assumed to behave isotropically. Film expansion was not allowed over the substrate borders in the lateral x and y directions to account for the film clamping condition. For modeling precipitates of different size, elastic properties of Nb were also used, since data for niobium hydride are missing. The local hydrogen-related lattice expansion of the precipitates was implemented by setting an initial strain of $\epsilon = 2.9\%$ to the precipitate in all three room directions. This value contains the bulk Nb-H expansion of $0.058c_H$ and a mean thin-film miscibility gap, $\Delta c_H = 0.5 \text{ H/Nb}$.²⁷ Sliding between precipitates and the film was not allowed. This border condition accounts for lattice coherency between the film and the precipitate, which is certainly true for initial states.²⁸ Shape, size, and positions of precipitates can be modified, and the resulting surface topography changes. The best fit of the results to the measured surface topography was obtained by using cylindrical precipitates, as discussed in detail in a recent paper.²⁸ In the current paper, we focus on the kinetics and, thus, the precipitate growth. The influence of the precipitates size and the film thickness on the surface topography of coherent precipitates is analyzed in detail.

IV. RESULTS

A. Experimental results

Typical surface topographies of the same Nb film before and after hydrogen exposure above the phase-transition pressure are shown in Fig. 1. For clarity, the surface topography is

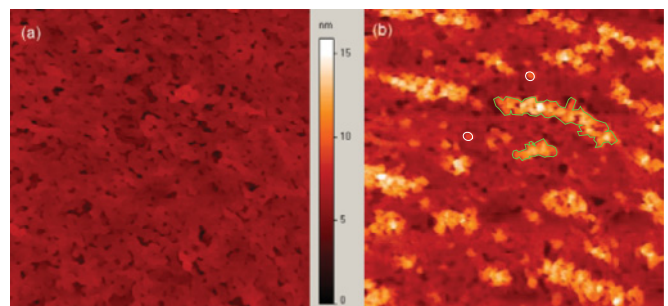


FIG. 1. (Color online) Topographical STM images of an 80 nm niobium-hydrogen film surface at different hydrogen gas pressures p_{H_2} and times: (a) $p_{H_2} = 2 \times 10^{-7}$ Pa; (b) after 67 h at $p_{H_2} = 9 \times 10^{-5}$ Pa the film surface shows surface topography changes. Locally elevated regions are visible. The substrate miscut is $< 0.1^\circ$ (image size: $2.5 \times 2.5 \mu \text{ m}^2$).

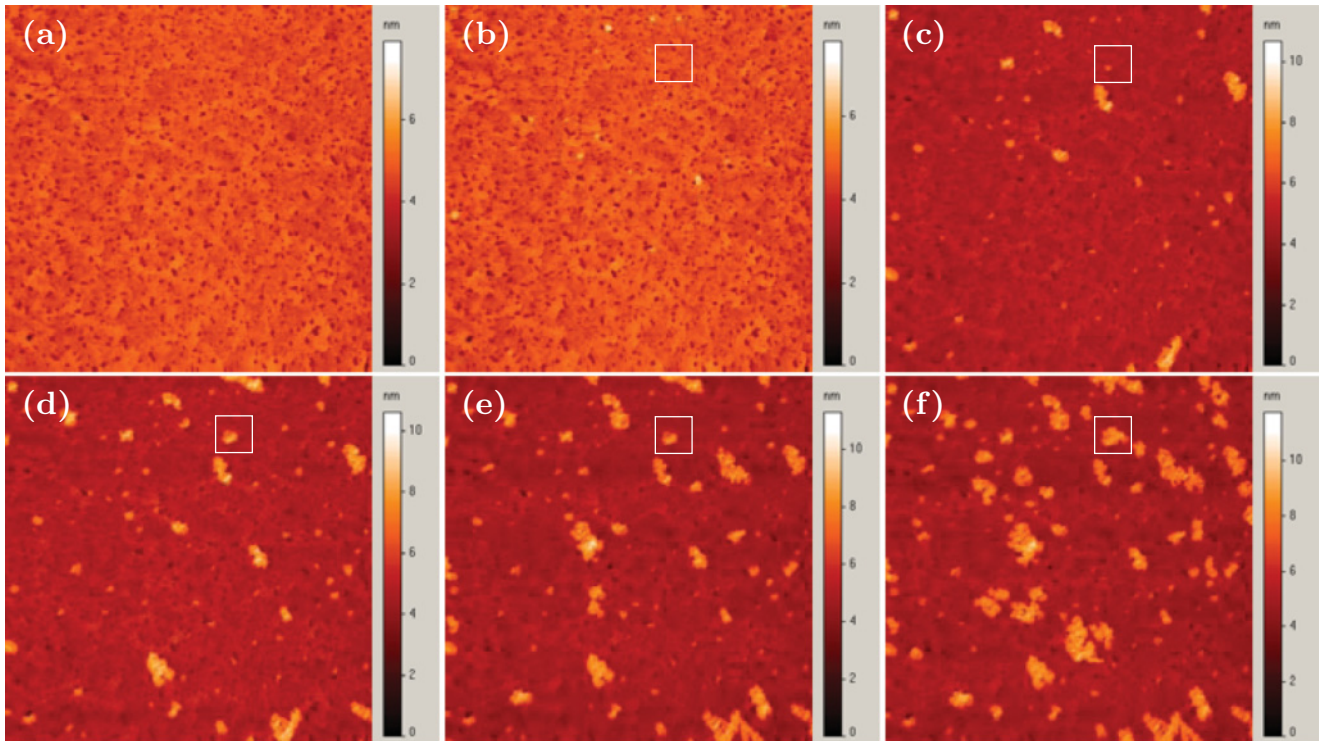


FIG. 2. (Color online) Hydride growth in a 70 nm thin niobium film as imaged with STM by surface topographies growth (T1 and T2). The images are chronologically taken at increasing hydrogen gas pressure. In (a) the as-prepared film is displayed. (b) First surface topography changes of type T1 are visible. In (c)–(f) the topographies expand and additional topographies of type T2 occur. The hydrogen gas pressure and measurement times are as follows: (a) before transformation, 3×10^{-5} Pa, (b) 4 min, 1×10^{-4} Pa, (c) 23 min, 1×10^{-4} Pa, (d) 43 min, 1×10^{-4} Pa, (e) 62 min, 1×10^{-4} Pa, and (f) 82 min, 2.5×10^{-4} Pa. The substrate miscut is $< 0.1^\circ$ (image size: $3.5 \times 3.5 \mu\text{m}^2$).

scaled to the same height of the color palette. This results in a rather uniform color for the as-prepared film in Fig. 1(a). After 67 h of the sample's exposure to hydrogen at 9×10^{-5} Pa, Fig. 1(b), the surface topography reveals elevated regions in comparison to the base level. Two different types of height topographies can be deduced in Fig. 1(b): flat circular-shaped topographies, named T1, and higher elongated topographies, named T2. Recently, we have shown that such surface topographies can be attributed to hydride formation inside the film.²⁸

Figure 2 demonstrates the chronological development of these topographies with time and a slight increase of the hydrogen partial pressure (a)–(f). The time axis is set to zero at the onset of hydrogen gas exposure. During the measurement, the pressure is slightly increased from 1×10^{-4} to 2.5×10^{-4} Pa to step up the phase transformation. For the first 23 min at $p_{\text{H}_2} = 1 \times 10^{-4}$ Pa, the number density of T1 increases [Figs. 2(b) and 2(c)]. Later on, it remains constant. A maximum height of 1.8(1) nm is determined for T1 topographies. The area fraction of T2 topographies continuously increases. The maximum height of T2 topographies is 4.7(5) nm. In Figs. 2(e) and 2(f), the growth rate of T2-related surface topographies is largely reduced compared to Figs. 2(c) and 2(d). The growth rate reduces to zero after long-time exposure under constant pressure conditions. While the lateral extension of circular T1 topographies is limited by a maximum radius of about 36(3) nm, T2 extends more or less linearly directed with time.²⁸

The surface topography height distributions of Fig. 2 are plotted in Fig. 3, showing the height information of all image pixels. Here, it is clearly visible that the height curve can be split into three individual topographies peaks: the base level, at $h = 0$ nm, keeps a constant position and simply shrinks in magnitude; the T1-related height peak is also situated at a constant height and only increases in intensity with exposure time; the T2-related height peak shifts and increases with exposure time. This figure clearly confirms the separation of T1 and T2 topographies.

The chronological size development of T1 and T2 topographies of Fig. 2 is addressed in more detail in the histogram of Fig. 3. Here, the number of surface topographies is counted as a function of the related surface area. For better comprehension, the related surface area is translated into an in-plane extension of surface topographies at the top axis of Fig. 3 by assuming a circular topography shape. Strictly speaking, such a translation is only applicable for T1 topographies and does not refer to the elongated T2 topographies.

For short times (b), the histogram monitors only small T1 topographies with a maximum area of about $0.006 \mu\text{m}^2$. This value relates to a maximum size of about 40 nm. A maximum number is detected for a mean area of $0.002 \mu\text{m}^2$ or a radius of less than 30 nm. Later on (c)–(f), the position of this maximum number shifts toward a value of about 36 nm. For these later stages (c)–(f), also larger topographies are counted, some extending over more than $0.07 \mu\text{m}^2$ (c) or up to $0.1 \mu\text{m}^2$. The number of these large topographies increases with time.

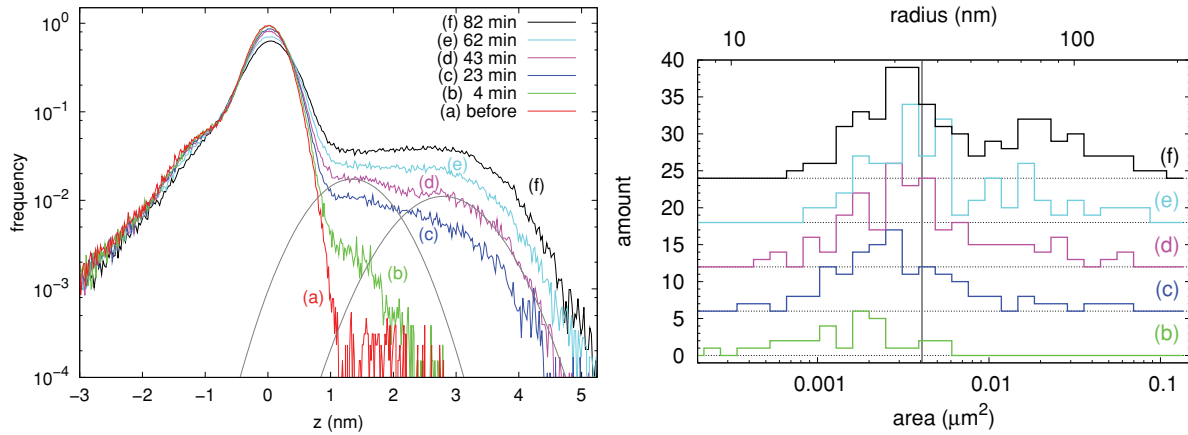


FIG. 3. (Color online) Left: Distribution of pixels heights of a 70 nm Nb film (Fig. 2). The base level is that of the α phase. Two clearly distinguishable additional height peaks, related to T1 topographies (b) or, also, T2 topographies are visible (c)–(f). The contribution of these peaks increases from (b) to (f). Right: Histogram of lateral extensions of surface topographies, determined from the STM images of Figs. 2(b)–2(f) for subsequent times. For short times only small T1 topographies exist (b). These topographies extend up to a maximum radius of 36 nm. The later stages (b)–(f) show a maximum surface topography number for this extension. Later stages also show large-size topographies, extending over more than 100 nm.

For all times, the histograms show a maximum at a radius of about 40 nm where the system seems to be locked in. For the stages (d)–(f), a second maximum develops at about $0.02 \mu\text{m}^2$, slightly shifting toward larger sizes with time.

Figure 4 shows details of the surface topography development with time for five subsequent hydrogen exposure times. These images, enlarged from Fig. 2 (the regions marked within the white box), reveal the typical time development of T1 topographies. It can be directly seen that for later stages, T2 topographies arise at the same position where T1 topographies were formerly detected.

The long-term surface topography of films is addressed in the following paragraph with regard to the influence of film thickness and substrate miscut. Typical surface topographies after long-time hydrogen exposure are shown in Figs. 5(a)–5(c) for a substrate miscut of less than 0.1° and (d) for a substrate miscut of less than 0.2° . For Figs. 5(a)–5(c), the film thickness increases, starting from (a) 20 nm, (b) 40 nm, to (c) 70 nm. The hydrogen partial pressure is about 1×10^{-4} Pa for all cases. The surface topography color height scale is different for the four images—this is of minor importance here since height scales are adjusted to properly image the individual surface topographies. Image (a) of the 20 nm film is, furthermore, a differential picture, focusing on the surface

topography changes with respect to the image taken before the H exposure.³⁴ Moreover, the exposure times differ since images are chosen to represent the long-term state.

For long-time exposure, the 20 nm film (a) shows only circular topographies, which we relate to T1. The 40 nm film (b) shows both circular (T1) and elongated (T2) topographies. The 70 nm film, finally, shows only elongated T2 topographies. A film of similar thickness, deposited on a substrate with stronger miscut, reveals a similar surface topography to (b), where both T1 and T2 topographies are visible. Thus, the images exhibit the following trend in the long-time surface topography: with the decrease of the film thickness, T1 are the dominant surface topographies. This trend is also observed for thick films when the substrate miscut is increased. On the contrary, the thick films surface image is dominated by T2 topographies, especially when the substrate miscut is small ($< 0.1^\circ$).

Transformation kinetics are addressed in the following paragraph by keeping the hydrogen partial pressure constant. The chronological development of T1 and T2 topographies is shown in Fig. 6. This measurement took about 7 days. During this time, more than 350 STM images were taken using the same STM tip. In an automated routine, the images were analyzed. Pixels with elevated height compared to the

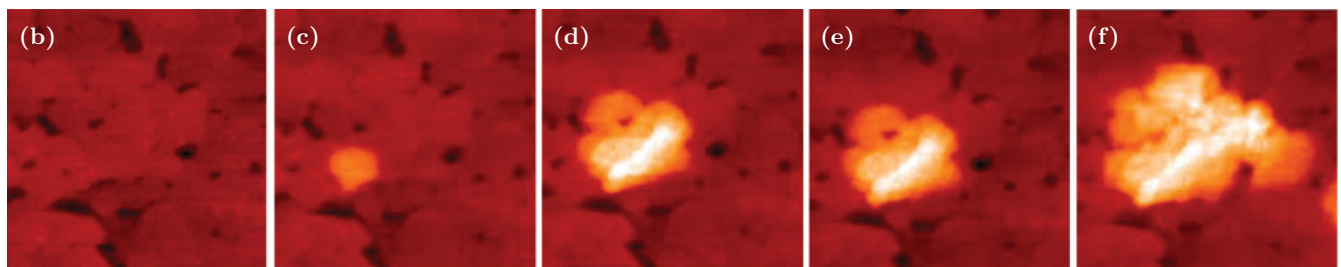


FIG. 4. (Color online) STM images of the topography development at one and the same surface position, enlarged from Fig. 2. T2 topographies originate from T1 topographies.

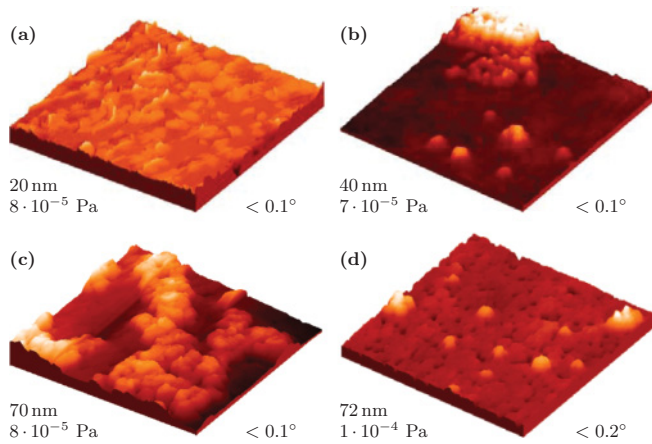


FIG. 5. (Color online) Long-term hydrogen exposure surface topographies of epitaxial Nb films of different thickness (a) 20 nm, (b) 40 nm, and (c)–(d) 70 nm and substrate miscut (a)–(c) $< 0.1^\circ$ and (d) $< 0.2^\circ$. The height scale varies from 0.5 nm in (a) to 5 nm in (d) (image size: $1 \times 1 \mu\text{m}^2$).

base level are separated by their magnitude. The histogram of height of each STM image (as exemplarily shown in Fig. 3) was fitted with three peaks, one for the unchanged pixel heights, another peak for the T1-related pixel heights, and the third peak for T2-related pixel height.

The total number of T1-related pixels and T2-related pixels with respect to the total number of image pixels is plotted in Fig. 6 as a function of time. Additionally, the total number of elevated pixels with regard to the base level is plotted. In the beginning, the number of T1-related pixels increases exponentially with time. The first stage is dominated by the formation and growth of T1 topographies, resulting in an increase of T1-topography pixel area. After about two days of hydrogen exposure, this increase diminishes and a constant

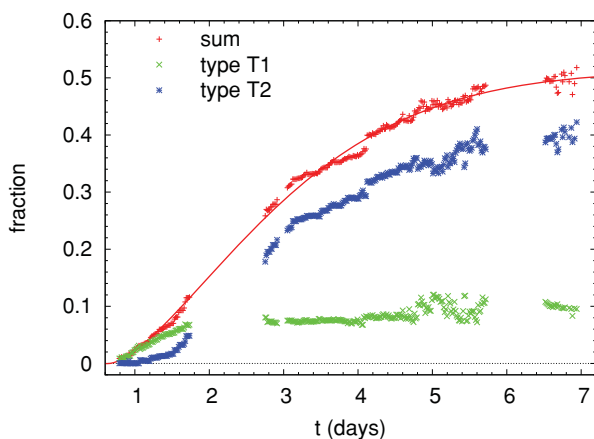


FIG. 6. (Color online) Time development of T1- and T2-surface topography areas of an 80 nm thin Nb film exposed to $p_{\text{H}_2} = 9 \times 10^{-5}$ Pa for about 7 days (for details, see the text). The sum of surface topography areas is also plotted. The time dependency can be fitted with an equation resorting to the model of Johnson, Mehl, Avrami, and Kolmogoroff. The area fraction saturates at 51.4(3)% of the total area. The Nb-H film transformation is, thus, locked in a certain transformation state.

and maximum surface fraction δ of T1 topographies is achieved with $\delta = 0.1$ of the total image area.

T2-topography-related pixels evolve with time. Their contribution is zero at the beginning and it increases after about one day with an S shape. The T2 contribution saturates after 5.5 days at a value of about 0.5 of the surface area. The time evolution of all elevated pixels, representing simply the sum of the T1- and the T2-accounted pixels, can be fitted to a model curve:

$$A(t) = 0.514(3) \times \left\{ 1 - \exp \left[- \left(\frac{t}{64.4(5)h} \right)^{1.50(2)} \right] \right\}. \quad (2)$$

The model curve describing the kinetics of the elevated area $A(t)$ resorts to the JMAK formula, Eq. (3). For long times t , this model curve converges to an area fraction of 0.514(3).

B. Finite-element simulation results

To study the expected surface corrugation (T1) for different film thickness originating from a coherent Nb hydride, FEM simulations were performed on cylindrical precipitates ranging through the complete film from the top to the film-substrate interface. This precipitate morphology was deduced for T1 topographies by comparing the FEM surface topographies with experimental T1-topography data.²⁸ The cylinder radius as well as the film thickness are varied and maximum surface corrugations are determined. This is shown in Fig. 7 for cylindrical precipitate with a 20 nm radius. The surface topography has a radius of about 28 nm and, thus, exceeds that of the cylinder. The maximum height of the surface corrugation of about 1.5 nm is achieved in the middle of the cylinder. Figure 8 summarizes the results. The maximum surface corrugation increases with cylinder radius. This increase does not depend on the film thickness. In addition, Fig. 7 reveals the internal strain state by coherent precipitation of a cylindrical Nb hydride. While the hydride is attached to the rigid substrate, lateral straining toward the matrix is possible above the substrate level.

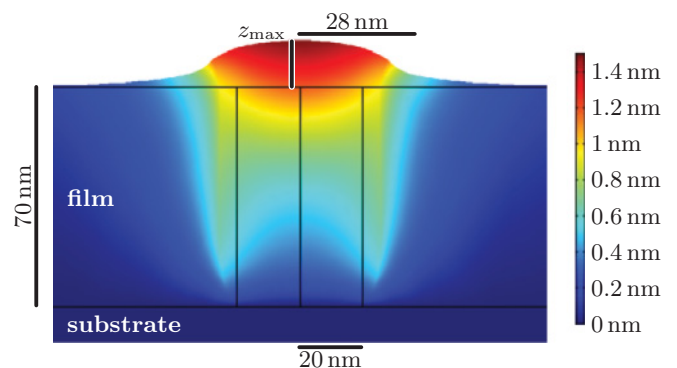


FIG. 7. (Color) Total displacement of a cylindrical precipitate calculated by the finite-element method. In this figure, a niobium film thickness of 70 nm was chosen and the precipitate radius was 20 nm. For better visibility, the plotted displacements are raised by a factor of 10. The maximal displacement $z_{\text{max}} = 1.5$ nm is shown in red, and areas with no displacement are indicated by blue.

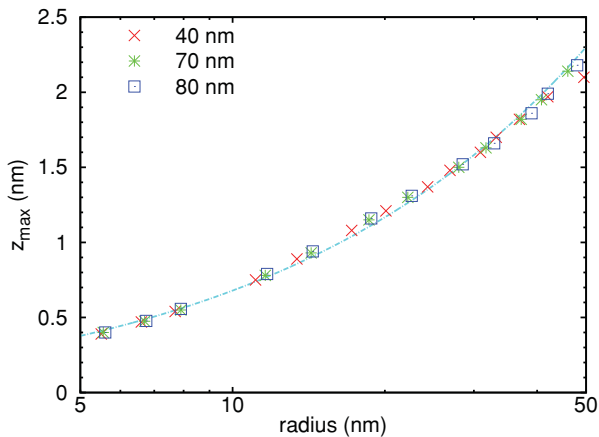


FIG. 8. (Color online) Surface corrugations of finite-element modulations on a coherently bound and expanded cylinder (model for the hydride) inside of a Nb thin film on a semi-infinite sapphire substrate. Lattice properties of bulk Nb and sapphire were implemented. The surface corrugation depends on the cylinder radius but not on the film thickness.

V. DISCUSSION

Hydrogen exposure to epitaxial Nb films at pressures above $6(1) \times 10^{-5}$ Pa results in surface topography changes that can be monitored by STM. The surface of the epitaxial film is smooth before hydrogen exposure. As soon as the pressure exceeds the hydride formation pressure for the thin film, a changed surface topography is measured.²⁸ Because the surface topographies appear after exceeding the hydride formation pressure, they can be directly related to the hydrided volumes in the film. Thus, surface topographies are just the visible top of hydrides inside of the film.

Two different types of surface topographies, T1 and T2, can be distinguished as shown in Fig. 3. From the bulk phase diagram, chemically just one hydride with 0.7 H/Nb is expected to form. For epitaxial thin films, the hydrogen concentration in the hydride is known to be reduced, as Dornheim *et al.* determined by XRD under controlled electrochemical loading conditions.³⁵ However, also, in the thin films only one hydride phase forms in this concentration range. This was confirmed by XRD measurements of Dornheim as well as, earlier, by Laudahn.^{21,27} Thus, it can be concluded that the hydride morphology and hydride lattice matching inside the film are responsible for the topographical differences between T1 and T2 at the film surface, and not the local chemistry.

In the sequence of Fig. 4 it was shown that T2 topographies arise at the same position where formerly T1 topographies were detected. From this position correlation between T1 and T2 topographies, it is suggested that T1-related hydrides (H1) are precursors of T2-related hydrides (H2).

In a recent work, we have shown that H1 and H2 hydrides inside the film are both cylindrical in shape and range through the complete film.²⁸ They only differ in their lattice matching: While H1 hydrides lay coherently in the matrix, H2 hydrides are semicoherently matched to the matrix. This interpretation was confirmed by finite-element calculation on an expanding cylinder (modeling the hydride) which was clamped to its sides (modeling coherency) and bonded to a stiff substrate

(modeling substrate conditions), giving exactly the measured T1 topography height profile.²⁸ For T2 topographies, such a matching was not possible. For all cases, the out-of-plane expansion of T2 topographies was much too large. But, the largest out-of-plane expansion measured for T2 topographies was in good accordance with results for a freely expanding precipitate (modeling an incoherent hydride) that was simply clamped to the semi-infinite substrate (modeling substrate conditions). Thus, we concluded that for this case, interfacial stress between the matrix and the precipitate was released by implementing dislocations.²⁸ All these interpretations are in good agreement with the time dependencies and the long-term surface topographies addressed in this work. Furthermore, they support the interpretation of H1 hydrides being precursors of H2 hydrides. In the framework of JMAK-theory, H1 hydrides may be regarded as growing nuclei. In these STM measurements, nuclei were detectable with a lowest radial size of 9 nm at the film surface. Smaller nuclei are not detectable at the specimen surface. This minimal detectable size was influenced by the resolution during the STM measurement. A pixel size of 4.5 nm was chosen to compromise on the image size and measurement time.

The hydride volume growth can be derived from Fig. 3. In early stages, just small (cylindrical) H1 hydrides are detected with a maximum radius of about 20–30 nm. For later stages, the size distribution becomes bimodal. The maximum size of the H1 hydrides increases slightly for later stages to about 30–40 nm. In addition, a second peak develops at larger areas marking the occurrence of H2 hydrides. This second H2-related peak shifts with exposure time reflecting the volume growth of the H2 hydrides. But, the H1-related peak seems to be locked at a radius of about 30–40 nm. This behavior we interpret with regard to the vertical lattice matching, which is coherent for H1. The coherency strain energy increases with the cylinder radius. It hinders further growth of cylindrical H1 at about 30–40 nm and keeps the hydride locked in this size. As soon as the energy is large enough to allow for the occurrence of a misfit dislocation and this dislocation can be generated, the coherency barrier vanishes and the hydride can grow. This growth is visible by the second peak (H2). The critical size for the generation of a misfit dislocation of 36 nm is shown in Fig. 3 by a vertical line.²⁸ The locked-in size obtained for 30–40 nm, thus, is interpreted as a hampered generation of misfit dislocations at the critical size.

The hydride-related topographies have certain lattice relations, which is clearly visible for the later stages of T2 topographies, as shown in Fig. 1. But, the positions where the T1-related hydrides form are not randomly distributed. The lattice relations are shown in Fig. 9 monitoring the orientation relation of T1 and T2 topographies with respect to the underlying Nb matrix. The Nb film orientation was obtained with regard to straight terrace edges and the vertical [110]-lattice direction. For a better visibility of small contributions, the rotational length axis is weighted by ξ^{-3} .^{36,37} Figure 9(a) reflects the positions dependency of each of the two T1 topographies being mainly in [111]-lattice directions. Figure 9(b) monitors the extension orientation relation of T2 topographies.

This can be interpreted with regard to the Nb lattice elastic properties being softest in [111]-lattice directions, as shown in

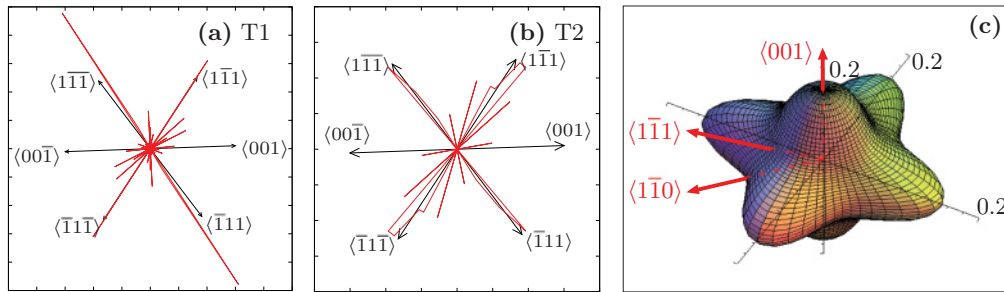


FIG. 9. (Color online) Orientation relations of (a) T1-surface topographies positions and (b) T2-surface topographies extensions with respect to the Nb film lattice. For comparison, part (c) shows the three-dimensional modulus of elasticity for Nb bulk in TPa. The Nb film orientation was determined by looking at terrace edges. Because of the functional dependency of elastic interactions, the topography distance or extension ξ is weighted by ξ^{-3} .^{36,37} (a) New T1-surface topographies preferentially form in special lattice directions, mainly of class [111]. (b) Also T2-topographies preferentially extend in these directions.

Fig. 9(c).³⁸ Here, the bulk modulus of elasticity is plotted in three dimensions, showing minima along the [111] directions. Hydride precipitation also yields small lateral expansions, as shown in the FEM simulation of Fig. 7. Atom positions are moved by about 1 nm apart from the film-substrate interface. Thus, hydride nucleation and hydride growth are expected to be energetically favorable along soft lattice directions.

In the next paragraph, the parameters influencing nucleation and growth of H1 and H2 hydrides are addressed with regard to the film surface and the interface properties. Figure 5 shows the dependency of the long-term surface topography on the film thickness, and the substrate miscut is shown. For thinner films and larger miscuts, mainly H1 hydrides were found. This finding can be interpreted with regard to the initial surface roughness. Under constant deposition parameters, such as temperature and rate, thinner films result in a rougher surface and pronounced surface steps and edges.³⁹ Also, an increasing substrate miscut leads to an increased number of surface steps in the as-prepared film. As these sites act as nucleation centers for heterogeneous nucleation, the number of nucleation sites is increased for both cases, and an increased number of T1 topographies, and consequently H1 hydrides, is measured.

Additional parameters influencing nucleation and growth of hydrides will be addressed by discussing the influence of the intrinsic dislocations and the Pd islands at the film surface. It can be assumed that the threading dislocations of the dislocation network act as heterogeneous nucleation centers for the hydride precipitates. But their quantity is much larger than the number of hydrides formed. Since the number of dislocations is similar for the 0.1° and 0.2° miscut films, but the H1 number strongly differs, the impact of the dislocation network on H1 nucleation is judged to be small. Nevertheless, it can be assumed that an edge component of the threading part of the dislocation network may act as a path for H1 extension, being responsible for the cylindrical shape of the hydrides.

The same argumentation holds for the impact of the Pd islands. Their size and density are kept constant for the different films even though the H1 and H2 appearances strongly vary. Furthermore, their number density is far larger than that of the hydrides. Therefore, we conclude also that Pd islands have a minor influence on hydride nucleation. According to these results, surface roughness turns out to have the strongest influence on the hydride formation.

The discussion in the following paragraph concentrates on the transformation kinetics shown in Fig. 6. As the hydrides have cylindrical shape and range through the complete film, the hydride-related surface topographies T1 and T2 can directly be transformed into a phase-transferred volume.⁴⁰ In the framework of JMAK kinetics, the number fraction of elevated pixels (T1 and T2) and the total pixel number, therefore, directly give the volume fraction of the phase-transferred volume. The chronological pixel development, or the fraction of the phase-transferred volume $X(t)$, is plotted in Fig. 6. It grows with the typical S-shape, and the total volume fraction follows a JMAK equation. But, because of an incomplete phase transformation, the JMAK equation is limited by the maximum volume fraction x_{\max} of transformed phase under the chosen conditions:

$$X(t) = x_{\max} \left\{ 1 - \exp \left[- \left(\frac{t}{\tau} \right)^n \right] \right\} \quad (3)$$

According to Eq. (2), the Avrami exponent is $n = 1.5$ and the maximum volume fraction is $x_{\max} = 51.4(3)\%$. This saturation value interestingly shows that, even under extreme long hydrogen gas exposures, the film does not transform completely into the hydride phase. The system is locked in an incomplete transformation state. This is different from the bulk, where, at a constant pressure above the hydride formation pressure, the whole sample transforms into the hydride by 100% once the transformation has started. For thin films, interestingly, this is no longer the case. We suggest that the mechanical stress that builds up during hydride precipitation has to be considered in a thermodynamic treatment of a thin film that is clamped to the rigid substrate. From an overall film measurement, Laudahn determined this stress to be compressive and in the range of several GPa.²¹ This stress contribution has to be added to the chemical potential of hydrogen in the metal. It increases the total chemical potential of hydrogen in the metal film during hydride precipitation. Just by increasing the chemical potential of the hydrogen gas, which is directly coupled to the hydrogen gas pressure by $\mu = \mu_0 + k \ln \frac{p}{p_0}$, the hydrogen uptake in the film can be increased. A higher outside hydrogen pressure is needed to force hydrogen into the thin film. This pressure should increase with precipitate content in the thin film.

The obtained Avrami exponent is now regarded with respect to the diffusion mechanism and the obtained kinetics. According to the table on diffusion-controlled growth, an Avrami exponent of 1.5 accounts for a decreasing nucleation rate.² But, taking the foil condition into account, which reduces the “true” Avrami exponent by up to 1, “true” Avrami exponents of up to $n = 2.5$ are possible. This means the nucleation rate can range from zero (1.5) through decreasing (1.5–2.5) to constant (2.5). However, an increasing nucleation rate (> 2.5) can be excluded.

The Avrami exponent n can be split into two different constituents, n_n for nucleation and n_g for growth. Also, in Fig. 6, a strong difference in the chronological development of H1 and H2 can be deduced: The volume fraction of H1 increases during the first 2 days and afterward stays constant. The volume fraction of H2 is negligible during the first day and increases strongly after 1.5 days. The H2 volume fraction tends to saturate after more than 5 days. This different behavior is somewhat suggestive of relating H1 to nuclei and H2 to growing precipitates.

If H1 hydrides were related to nuclei, a decreasing and then constant nucleation rate could be directly gained by looking at the T1 development in Fig. 6: The T1 contribution increases during the first 2 days, then the number density is constant—in total the T1 nucleation rate would decrease to a constant value. But H1 hydrides also grow, and the increase of the H1 volume fraction also implements H1 growth. Thus, the H1 development just provides a trend. However, this experimental detail is in good agreement with the experimentally obtained Avrami exponent and its theoretical interpretation.

VI. SUMMARY

Hydride precipitation and growth in epitaxial Nb films deposited onto sapphire substrates was studied by locally monitoring the film surface. At hydrogen pressure above 6×10^{-5} Pa, first coherent hydrides (H1) of cylindrical

morphology form. They range from the film surface to the film-substrate interface. These hydrides grow up to a cylinder radius of 30–40 nm, where coherency stress between the matrix and the hydride hinders further growth. Above 36 nm, the strain energy exceeds that of a misfit dislocation. Once this dislocation is generated, the hydride can grow, resulting in semicoherent H2 hydrides. The exact position of dislocation loop generation is still unknown. Future *in situ* TEM investigations might address this point, but as of yet such measurements have not been reported. The H2 hydrides predominately grow in elastically soft [111] lattice directions, resulting in elongated H2 morphologies. Also predominately in these directions, H1 hydrides tend to nucleate.

Surface roughness was found to influence strongly the relation between H1 and H2 occurrence. This was attributed to an increased number of offered nucleation sites.

Hydride transformation kinetics under constant pressure conditions were described by a JMAK-type model. It was found that for Nb-H films, the phase transformation saturates in an incomplete transformation state and is, thereby, locked at about 50% of the hydrided film volume. In comparison to bulk Nb, where above the hydride formation pressure the sample turns completely into a Nb-H hydride phase, only partial precipitation of the hydride phase is observed in the Nb films, attributed to the stress arising from the clamped state of the film on a rigid substrate. This mechanical stress increases the chemical potential for hydrogen in the Nb film. As a result, a higher hydrogen gas pressure is needed to drive more hydrogen into the thin film. The interpretation of the obtained Avrami exponent could be directly linked to the kinetic development of H1 and H2 hydrides.

ACKNOWLEDGMENTS

The authors would like to thank the Deutsche Forschungsgemeinschaft for financial support via SFB 602 (project A9 and B12).

*apundt@ump.gwdg.de

¹A. Pundt and R. Kirchheim, *Annu. Rev. Mater. Res.* **36**, 555 (2006).

²J. W. Christian, *The Theory of Transformations in Metals and Alloys* (Oxford, Pergamon, 1965).

³A. N. Kolmogoroff, *Izv. Akad. Nauk SSSR, Ser. Matem.* **3**, 355 (1937).

⁴W. A. Johnson and R. F. Mehl, *Trans. Am. Inst. Min. Eng.* **135**, 416 (1939).

⁵M. Avrami, *J. Chem. Phys.* **8**, 212 (1940).

⁶M. Tomellini and M. Fanfoni, *Phys. Rev. B* **55**, 14071 (1997).

⁷V. Erukhimovitch and J. Baram, *Phys. Rev. B* **50**, 5854 (1994).

⁸V. Erukhimovitch and J. Baram, *Phys. Rev. B* **51**, 6221 (1995).

⁹C. Michaelsen, M. Dahms, and M. Pfuff, *Phys. Rev. B* **53**, 11877 (1996).

¹⁰M. Fanfoni and M. Tomellini, *Il Nuovo Cimento* **20 D**, 1171 (1998).

¹¹M. Scott, in *Amorphous Metallic Alloys*, edited by F. E. Luborsky (Butterworth, London 1983).

¹²T. Car, N. Radicacuta, J. Ivkov, and A. Tonejc, *Appl. Phys. A* **80**, 1087 (2005) [<http://www.springerlink.com/content/awkke2dnem3286m/>].

¹³Z. Ma and L. H. Allen, *Phys. Rev. B* **49**, 13501 (1994).

¹⁴C. Michaelsen, K. Barmak, and T. P. Weihs, *J. Phys. D* **30**, 3167 (1997) [<http://www.iop.org/EJ/abstract/0022-3727/30/23/001>].

¹⁵C. Michaelsen, *Philos. Mag. A* **72**, 813 (1995).

¹⁶*Gase und Kohlenstoff in Metallen*, edited by E. Fromm and E. Gebhardt (Springer-Verlag, Berlin, 1976).

¹⁷S. Wagner and A. Pundt, *Appl. Phys. Lett.* **92**, 051914 (2008).

¹⁸*Hydrogen in Metals I*, edited by G. Alefeld and J. Völk, Topics in Applied Physics Vol. 28 (Springer-Verlag, Berlin, 1978).

¹⁹B. J. Makenas and H. K. Birnbaum, *Acta Metall.* **28**, 979 (1980).

²⁰T. Schober, *Scr. Metall.* **7**, 1119 (1973).

²¹U. Laudahn, A. Pundt, M. Bicker, U. von Hülsen, U. Geyer, T. Wagner, and R. Kirchheim, *J. Alloys Compd.* **293–295**, 490 (1999).

- ²²G. Andersson, B. Hjörvarsson, and H. Zabel, *Phys. Rev. B* **55**, 15905 (1997).
- ²³H. Zabel and A. Weidinger, *Comments Condens. Matter Phys.* **5**, 239 (1995).
- ²⁴Q. M. Yang, G. Schmitz, S. Fähler, H. U. Krebs, and R. Kirchheim, *Phys. Rev. B* **54**, 9131 (1996).
- ²⁵T. Massalski, *Binary Alloy Phase Diagrams* (American Society for Metals, Metals Park, OH, 1986).
- ²⁶J. A. Pryde and C. G. Titcomb, *Trans. Faraday Soc.* **65**, 2758 (1969).
- ²⁷M. Dornheim, Ph.D. thesis, Georg-August-Universität zu Göttingen (2002).
- ²⁸K. Nörthemann and A. Puntdt, *Phys. Rev. B* **78**, 014105 (2008) [<http://link.aps.org/abstract/PRB/v78/e014105>].
- ²⁹A. R. Wildes, J. Meyer, and K. Theis-Bröhl, *Thin Solid Films* **401**, 7 (2001).
- ³⁰E. J. Grier, O. Kolosov, A. K. Petford-Long, R. C. C. Ward, M. R. Wells, and B. Hjörvarsson, *J. Phys. D* **33**, 894 (2000).
- ³¹D. M. Tricker and W. M. Stobbs, *Philos. Mag.* **71**, 1051 (1995).
- ³²K. Nörthemann, R. Kirchheim, and A. Puntdt, *J. Alloys Compd.* **356–357**, 541 (2003).
- ³³COMSOL MULTIPHYSICS version 3.2, www.comsol.com, with "Structural Mechanics Module."
- ³⁴This image treatment was needed because the 20 nm thin film has a larger roughness compared to the thicker films making hydrogen-induced surface changes hardly visible in the pure surface topography image.
- ³⁵M. Dornheim, N. Jisrawi, K. Nörthemann, O. Dankert, J. Cizek, J. Bankmann, C. Bähz, and M. K. und A. Puntdt, *Hamburger Synchrotron Labor Annual Report* (2001), p. 907.
- ³⁶A. G. Khachatryan and G. A. Shatalov, *Sov. Phys. Solid State* **11**, 118 (1969).
- ³⁷H. Yamauchi and D. De Fontaine, *Acta Metall.* **27**, 763 (1979).
- ³⁸K. H. Hellwege and O. Madelung, *Zahlenwerte und Funktionen aus Naturwissenschaften und Technik*, Landolt Börnstein, Vol. 18 (III) (Springer-Verlag, Berlin, 1984).
- ³⁹M. Oehring, *The Materials Science of Thin Films* (Academic, London, 1991).
- ⁴⁰This translation implements a small error due to the smaller size of the hydride with respect to the surface topography shown in Fig. 7. This error is relatively larger for smaller precipitates and results in an overestimation of the transformed volume.